

No-drift phase-change memory alloy for neuromorphic computing

Xiaozhe Wang^{1,*}, Ruobing Wang^{2,*}, Suyang Sun^{1,*}, Ding Xu¹, Chao Nie¹, Zhou Zhou¹, Chenyu Wen¹, Junying Zhang¹, Ruixuan Chu¹, Xueyang Shen¹, Wen Zhou¹, Zhitang Song², Jiang-Jing Wang^{1,*}, En Ma^{1,*}, Wei Zhang^{1*}

¹Center for Alloy Innovation and Design (CAID), State Key Laboratory for Mechanical Behavior of Materials, Xi'an Jiaotong University, Xi'an, 710049, China.

²National Key Laboratory of Materials for Integrated Circuits, Shanghai Institute of Microsystem and Information Technology, Chinese Academy of Sciences, Shanghai 200250, China

*These authors contributed equally to this work.

*Emails: j.wang@xjtu.edu.cn, maen@xjtu.edu.cn, wzhang0@mail.xjtu.edu.cn

Abstract:

Spontaneous structural relaxation is intrinsic to glassy materials due to their metastable nature. For phase-change materials (PCMs), the resultant temporal change in electrical resistance seriously hamper in-memory computing (IMC) applications. Here, we report an ab-initio-calculation-informed design of amorphous PCM composed of robust “molecule-like” motifs with minimal Peierls distortion, depriving the amorphous alloy of structural ingredients that would gradually evolve upon aging to entail resistance drift. We demonstrate amorphous CrTe₃ thin films that display practically no resistance drift at any working temperature from -200 to 165 °C. We achieve multilevel programming of CrTe₃ through both step-wise crystallization and step-wise amorphization using a hybrid opto-electronic device at various temperatures. Moreover, the application potential of CrTe₃ in neuromorphic computing is testified by its incorporation in a vehicle with automatic path-tracking function. Our work opens a new avenue to achieving IMC-requisite properties via judicious design of the composition and atomic-level structure of disordered PCM alloys.

Data-intensive applications, such as Artificial Intelligence (AI) and the Internet of Things (IoT), are having a profound impact on nearly all aspects of life. The huge amount of data being generated at an ever-increasing rate poses formidable challenges to efficient data storage and processing. Neuromorphic computing or in-memory computing (IMC) based on resistive-switching nonvolatile memory (NVM) arrays, unifying storage with computing at the same location, can substantially improve the computing efficiency at a much lower energy cost¹⁻⁴. The key to high-storage-density neuromorphic computing is to obtain as many distinguishable resistance levels as possible in every memory/computing cell⁵. Yet, high-precision IMC is facing a bottleneck problem associated with the intrinsic randomness of materials upon programming⁶, especially when operated at a working temperature (T) different from room temperature (RT). Continuous cooling is feasible at power farms, but for the power-limited edge computing platforms, temperature effects⁷⁻⁹ on accurate multilevel programming are much more critical.

Chalcogenide phase-change materials (PCMs), which utilize the large resistance contrast between their amorphous and crystalline states for data encoding^{10,11}, are one of the leading candidates for NVM. The flagship Ge₂Sb₂Te₅ (GST) alloys with moderate doping¹² or heavy alloying¹³ have enabled industrial production of high-density 3D Cross Point memory cards for computing servers and data centers with an operating T of 60~80 °C, as well as embedded memory units for automotive with a working T of -40~165 °C¹⁴. Very recently, it has also been shown that crystalline and amorphous PCM can survive the harsh space environment outside of the International Space Station¹⁵, where temperature can cycle between -120 and 120 °C 16 times per day. Beyond the success in these binary storage applications, PCMs do show multilevel storage capacity. But the spontaneous structural relaxation – aging – of amorphous PCM causes intolerable resistance drift¹⁶⁻¹⁸. This is a pressing problem threatening the device accuracy needed for neuromorphic computing applications¹⁹.

Massive research efforts have been devoted to overcoming the adverse impact of resistance drift. On the device side, several approaches using mixed-precision computing¹⁹, algorithm compensation²⁰, metal liner confinement²¹ and multi-PCM units²² were developed to partially mitigate the drift problem. It remains unclear whether these workaround solutions can still function at elevated temperatures or upon extreme temperature cycling, but in any case, they add complexities to high-density device manufacturing and accurate multilevel programming. Therefore, a fundamental solution

on the materials side, i.e., PCMs with intrinsically low drift and randomness, are sorely needed. Previous attempts employing impurity doping, heterostructure confinement and down-scaling the film thickness only managed to reduce the drift tendency at RT²³⁻²⁹. However, there is so far no candidate PCM that can generate thousands of robust resistance states to function across a wide range of operating temperatures for various application scenarios. In the following, we offer a materials solution to diminish relaxation/drift once and for all, via a paradigm shift towards “molecular-glass-like” amorphous PCMs (a-PCMs). This approach enabled us to discover an a-PCM that is intrinsically insusceptible to resistance drift at all working temperatures practically encountered in IMC operations.

Design of “molecular-glass-like” a-PCM

Upon aging, a-PCMs are subject to structural relaxation. Conventional a-PCMs experience a gradual (i) reinforcement of Peierls distortion of (defective) octahedral motifs³⁰ and (ii) disappearance with increasing time (t) of salient structural defects³⁰⁻³², including "wrong" bonds (e.g. Ge–Ge homopolar bonds) and tetrahedral motifs. Both of these two factors result in resistance drift. Our key idea is then to find an a-PCM that intrinsically has no such tendencies during the time- and temperature-induced relaxation. We first noticed that Peierls distortion is nearly non-existent in all crystalline polymorphs of $3d$ transition metal (TM) tellurides at Te-rich compositions ($\text{Te:TM} \geq 2:1$), where each $3d$ transition metal atom is coordinated by six Te atoms, forming an octahedral motif with symmetric bonding along each direction. Although the octahedral motifs can be slightly distorted, with the Te-TM-Te bond angle being slightly smaller or larger than 90° , there is no long/short bond correlation to establish *bona fide* Peierls distortion (see Supplementary Fig. S1). We conjectured that this scenario could be retained to the amorphous counterpart of such tellurides. Given the Te-rich composition, the probability to form wrong (TM-TM) bonds in the amorphous state is also reduced. It is then promising that the two factors (i) and (ii) in the preceding paragraph can be minimized.

To this end, we scrutinized all $3d$ transition metal tellurides. Among them, CrTe₃ is the richest in Te composition. Fig. 1a shows the relaxed crystalline (c-) CrTe₃ calculated via spin-polarized density functional theory (DFT). First, the directional bonds of c-CrTe₃ show no obvious Peierls distortion; the bond lengths are nearly identical, and the maximum difference is as small as 0.03 Å, an order of magnitude smaller than that of rhombohedral GeTe, ~0.4 Å. Second, the crystal shows a layered

structure composed exclusively of corner- and edge-sharing [CrTe₆] octahedra. It is thus well possible that its amorphous phase (a-CrTe₃) would also contain a very high density of non-defective [CrTe₆] octahedra with little Peierls distortion. To see if this hypothesis pans out, we carried out DFT-based ab initio molecular dynamics (AIMD) calculations to obtain a-CrTe₃ models of 200 atoms following a standard melt-quenched approach. We first used the computed crystalline density directly, and the obtained atomic structure is shown in Fig. 1a. As highlighted using coordination polyhedra, almost all Cr atoms indeed form [CrTe₆] octahedra (48 out of 50 Cr atoms, and the rest 2 Cr octahedra have only one missing neighbor). This observation is further confirmed by quantitative structural analyses shown in Supplementary Fig. S2a.

We next evaluated the degree of Peierls distortion in the amorphous counterpart, i.e., a-CrTe₃ model, by calculating the angular limited three-body correlation (ALTBC) at RT (~25 °C) over directional bonding pairs (bond angle ~155–180°). In stark contrast with conventional PCM with an extended wing-shape³⁰, a-CrTe₃ displays a single primary peak around 2.72 Å in the ALTBC profile at RT (Fig. 1b), which matches that of the c-CrTe₃ (marked by black circle). We also calculated the ALTBC profiles of a-CrTe₃ at other (lower and higher than RT) temperatures (Supplementary Fig. S2b), and they show a picture consistent with that at RT. Further optimization of the amorphous model at RT leads to a volume expansion by ~2.1%, but the structural features remain the same (see Supplementary Fig. S2c). Four additional a-CrTe₃ models in both crystalline and amorphous density were calculated, which confirm that a-CrTe₃ is consisted of [CrTe₆] octahedra connected in a disordered fashion, without obvious Peierls distortion and structural defects. In fact, octahedra are the only local configuration observed, and these motifs can hence be deemed “molecule-like”. We prolonged the cooling time by a factor of two and three in forming a-CrTe₃, and this structural feature remained the same (Supplementary Fig. S3).

With the desired structural features in hand, the next challenge is the requisite electronic properties. For IMC applications, it is imperative for the PCM to have a large contrast window in electrical resistance upon switching. The computed electronic density of states (DOS) does predict a major difference in electronic structure between c-CrTe₃ and a-CrTe₃ (Fig. 1c). The crystalline phase is a semiconductor stabilized by antiferromagnetic interactions³³. For the amorphous phase, we considered a couple of magnetic configurations, and the band gap is always filled. Fig. 1c shows the

DOS for the ferromagnetic state, and other magnetic configurations are included in Supplementary Fig. S4. The open versus filled band gap should result in a sizable difference in electrical resistivity between the two states, with the amorphous state being the lower-resistance state, which was observed in a similar layered PCM, CrGeTe₃^{34,35}. Importantly, as noted in Supplementary Fig. S2, the same octahedral configuration (“molecules” as well as their number density) stays predominant at elevated temperatures, suggesting that the a-PCM should also have an excellent thermal stability across a wide range of operating temperatures.

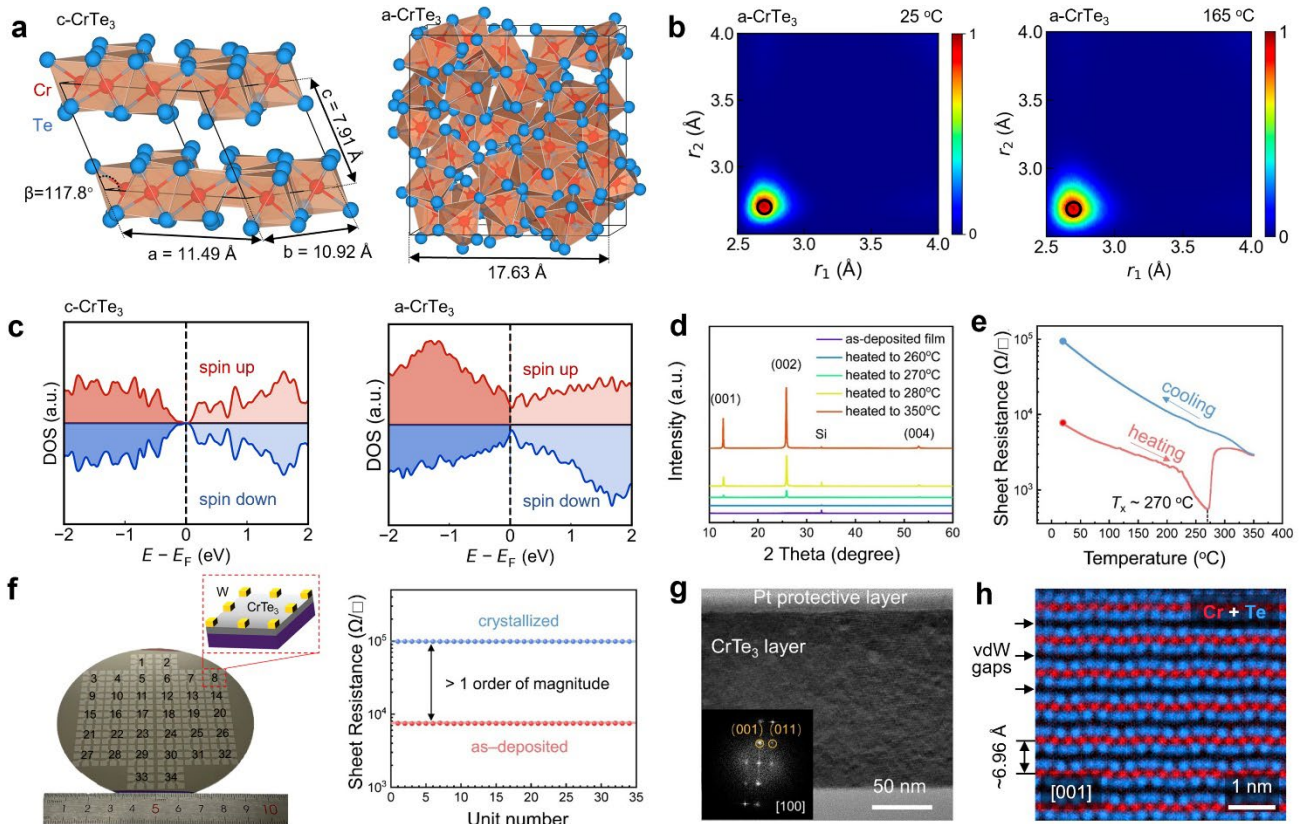


Fig. 1 | Materials design, synthesis and characterizations. (a) The relaxed atomic structures of c-CrTe₃ and melt-quenched a-CrTe₃. The Cr and Te atoms are rendered with red and light blue spheres and the [CrTe₆] octahedra are highlighted by orange polyhedra. (b) The ALTBC plot of a-CrTe₃ showing no Peierls distortion at ~25 °C and ~165 °C. The black circle indicates equal bonds in c-CrTe₃ (~2.7 Å). (c) The calculated DOS of c- and a-CrTe₃. (d) The XRD patterns of the as-deposited thin film and the thin films heated to 260 °C, 270 °C, 280 °C and 350 °C, respectively. (e) The temperature dependence of sheet resistance of CrTe₃ film heated up to 350 °C with a heating rate of 10 °C /min, and was then cooled to RT. (f) The van der Paul measurement of 34 units on a 4-inch wafer. The 0.5 × 0.5 cm² CrTe₃ area in the middle of the substrate is contacted by 8 tungsten electrodes (marked in yellow), which were patterned at the edges of the 1.2 × 1.2 cm² substrate. (g) The TEM bright-field image and (h) the atomic-scale elemental mapping of c-CrTe₃. The positions of the Te and Cr columns are marked in blue and red, respectively.

Wafer-scale synthesis of high-quality CrTe₃ films

We deposited CrTe₃ thin films of ~50–150 nm in thickness on 4-inch-diameter SiO₂/Si substrates at RT, using a pure Cr target and a pure Te target via magnetron sputtering. A ~10 nm thick ZnS-SiO₂ capping layer was grown on top of the CrTe₃ film inside the vacuum chamber to prevent oxidation and evaporation. Then we heated several ~150 nm as-deposited thin films up to 260 °C, 270 °C, 280 °C and 350 °C, respectively, with a heating rate of 10 °C /min. For the as-deposited film and the one heated to 260 °C, X-ray diffraction (XRD) patterns at RT (Fig. 1d) show no crystalline diffraction peaks, except for the silicon substrate. For higher annealing temperatures, c-CrTe₃ peaks of (100), (200) and (400) appeared, indicating that these thin films formed an out-of-plane texture. The lattice parameters obtained by XRD are 11.53, 11.19 and 7.79 Å, in good agreement with DFT calculation, 11.49, 10.92 and 7.91 Å. From the relatively sharp XRD peaks, the size of grains appears to be at least several hundreds of nanometers. As estimated from X-ray reflectometry (XRR), the mass density of the as-deposited amorphous film was ~6.12 g/cm⁻³, and was increased to ~6.39 g/cm⁻³ upon crystallization (Extended Data Fig. 1a), corresponding to a density increase ($\Delta\rho/\rho_{\text{crystal}}$) of ~3.9%, which is smaller than that of GST, ~6.4%³⁶.

Next, we measured the electrical resistance of the as-deposited thin film upon *in situ* heating to 350 °C with a heating rate of 10 °C / min using the van der Pauw method in an Argon-protected environment. In agreement with our DFT prediction, Fig. 1e shows an inverse resistance contrast upon crystallization for CrTe₃, opposite to GST. The sheet resistance of the as-deposited film was ~7 kΩ/◻ at RT, gradually decreasing upon heating. Starting from ~230 °C, the sheet resistance dropped more quickly, reaching a minimum at $T_x \sim 270$ °C, where crystallization started, which is consistent with the XRD data. The sheet resistance of the crystallized film was measured to be 100 kΩ/◻ at RT. According to the Hall effect measurements, the carrier concentration and mobility of the as-deposited film were 5.1×10^{20} cm⁻³ and 6.8×10^{-1} cm² V⁻¹ S⁻¹, respectively, which were reduced to 6.6×10^{19} cm⁻³ and 2.8×10^{-1} cm² V⁻¹ S⁻¹) in the crystallized film. To assess the reproducibility, we fabricated 34 tungsten-electrode-based test cells, each containing eight electrodes, and measured their sheet resistance of the as-deposited amorphous phase and the crystallized phase at 350 °C. All the 34 test cells gave highly consistent resistance values (Fig. 1f).

We carried out transmission electron microscopy (TEM) experiments to gain a microscopic view

of the crystallized phase. As shown in Fig. 1g, the cross-sectional bright-field image looks homogeneous with limited intensity contrast, and no grain boundary can be observed at this magnification. The Fast Fourier Transform pattern (FFT) confirms the crystal orientation of the c-CrTe₃ film to be [001]. The zoom-in TEM images taken at locations from the top to the bottom of the film consistently show well-aligned (001) lattice planes parallel to the substrate surface (Extended Data Fig. 1b), consistent with the XRD results, indicating epitaxial-growth-like crystal quality even though no seeding layer was used in the deposition. The scanning transmission electron microscopy – high-angle annular dark field (STEM-HAADF) image and the corresponding elemental mapping images show a clear arrangement of slabs of CrTe₃ trilayers sandwiching van der Waals (vdW) gaps, see Fig. 1h and Extended Data Fig. 1c. We thoroughly checked the structural features at different locations, confirming the highly textured large grains across the 4-inch c-CrTe₃ thin film (Extended Data Fig. 1c). The electron-transparent region in the TEM foil (lateral dimension >5 μm) of the 50-nm c-CrTe₃ thin film (Extended Data Fig. 1d) is nearly a single grain. This structural uniformity leads to highly consistent resistance values across the whole silicon wafer (Fig. 1f).

Suppressed resistance drift at extreme temperatures

The resistance drift behavior of amorphous PCMs is usually characterized using $R(t) = R_0(t/t_0)^v$ ($\sigma(t) = \sigma_0(t/t_0)^{-v}$), where R_0 (σ_0) is the resistance (conductance) measured at the time t_0 , and v is the drift coefficient over time t . To avoid potential aging effects due to sample storage, we measured the resistance of a-CrTe₃ thin films immediately after their sputter preparation. We tested different film thickness from 50 to 150 nm, which all showed an ultralow drift with $v \sim 0.001$ at RT. With a drift coefficient of this level, resistance drift would have little impact on practical multilevel programming.

In what follows, we focus on the film of 50 nm, as such film thickness is more suitable for multilevel programming in our devices. Fig. 2a displays the as-deposited a-CrTe₃ thin film heated to increasingly elevated temperatures in a sequential order, and at each temperature the holding time was 1 hour. The a-CrTe₃ thin film showed a consistently low v of 0.001–0.002 between RT and 150 °C. At 165 °C, its v slightly increased to ~0.004. These values are far smaller than that of a-GST, $v \sim 0.11$ between RT and 100 °C (Supplementary Fig. S5). Another issue of a-GST is that it crystallizes quickly at higher temperatures (e.g., when approaching 150 °C), making it unsuitable for embedded memory

applications. The ultralow drift behavior of a-CrTe₃ was also found to be robust over much longer time. We took two other fresh as-deposited thin films, and recorded their sheet resistance at 25 °C and 150 °C over 10 hours, respectively. Then the two films were stored for three days in air without Argon protection at RT. Subsequently, the two films were measured again at 25 °C and 150 °C over another 10 hours. Both sets of a-CrTe₃ films showed $v \sim 0.001$ (Fig. 2b). It is noted that transition metal atoms are typically reactive, and they can still be oxidized despite the presence of the capping layers. But for CrTe₃, all Cr atoms form strong bonds with Te atoms in compact octahedra, presenting a good air stability.

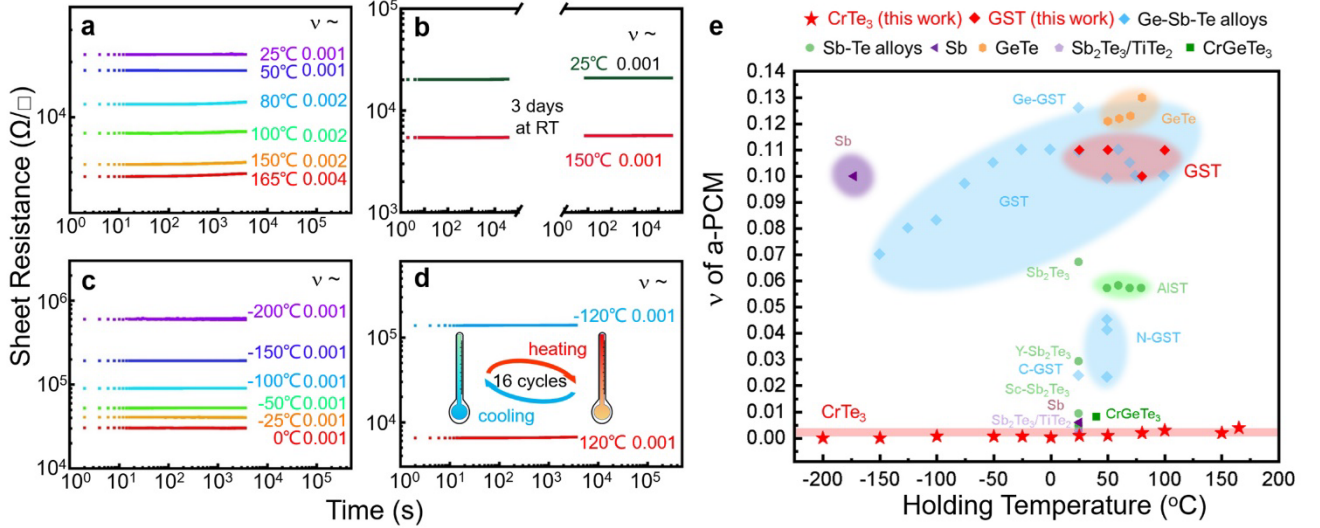


Fig. 2 | Suppression of resistance drift. (a) The resistance drift measurement of as-deposited a-CrTe₃ film upon heating over 1 hour at different holding temperatures. (b) Two as-deposited a-CrTe₃ films were measured at 25 and 150 °C over 10 hours (first part). After aging for 3 days at RT, they were measured at 25 and 150 °C over 10 hours again (second part). (c) The resistance of a-CrTe₃ film measured at 0 °C and below. (d) The a-CrTe₃ film was subjected to an extreme temperature cycling between -120 °C and 120 °C over 16 times in 24 hours, and subsequently its sheet resistance was measured at -120 °C and 120 °C over time. The distinctive resistance levels were due to the varied thermally excited carrier concentration at different temperatures. (e) A summary figure of drift coefficient of various amorphous PCM. The drift coefficient is highly temperature-dependent, e.g. v of a-Sb can be enlarged from ~ 0.001 at RT to ~ 0.1 at -173 °C.

We also tested the drift behavior of a-CrTe₃ at much lower temperatures. Our home-made setup was used to record the resistance at 0 and -25 °C, whereas a physical property measurement system (PPMS) utilizing the liquid helium refrigeration was employed to measure the resistance change at even lower temperatures. As shown in Fig. 2c, our a-CrTe₃ film again displayed very steady resistance with little drift, $v \sim 0.001$, from 0 °C down to -200 °C. We also confirmed that such minimal drift can

be sustained upon extreme temperature cycling. We heated an as-deposited CrTe₃ thin film to 120 °C, and then cooled it down to −120 °C (heating/cooling rate of 5.4 °C/min). Such thermal cycling was performed for a total of 16 times within 24 hours. The resistance of the film was then measured at 120 °C and −120 °C, respectively. As shown in Fig. 2d, the ultralow drift remained unchanged, $v \sim 0.001$.

To ascertain the melt-quenched a-CrTe₃ displays the same no-drift behavior, we carried out electrical measurements on a series of confined memory devices. As shown in Fig. 3a, one CrTe₃ cell was thermally annealed at 350 °C to form a full crystalline state, and was programmed to a full amorphous state using a single electrical pulse. The drift coefficient ($v \sim 0.001$) determined from the data acquired immediately after the electrical melt-quench (see also the Supplementary Video 1) is consistent with the behavior of as-deposited amorphous phase. The subsequent cross-sectional TEM characterizations confirmed that the electrical switching rendered the cell fully amorphous. We also performed cycling measurements and found the same no-drift behavior of the RESET state after 2×10^5 cycles (Fig. 3b). The same electrical measurements were repeated for several additional cells, and the drift coefficient values of both the initial RESET and the final RESET states are consistently close to 0.001 (Extended Data Fig. 2).

We now summarize in Fig. 2e the drift coefficient v of a-CrTe₃ (red stars) together with various amorphous PCMs^{23–29,37–39}, plotted versus holding temperatures. Previous drift measurements of a-PCMs, including the best-so-far TiTe₂/Sb₂Te₃ heterostructure²⁶, were mostly conducted at RT. The holding T was limited to ~100 °C, due to their relatively low T_x . Doping and alloying can increase the thermal stability of the amorphous phase, which, however, can also result in resistance drift in the crystalline phase with v reaching ~0.01 or even higher³⁹. By contrast, for our c-CrTe₃ (Extended Data Fig. 3), the sheet resistance showed a consistently low $v \sim 0.001$ at all the holding temperatures used for a-CrTe₃. Scaling the film thickness down to several nm in general helps to reduce v at RT³⁷, but it would be difficult to generate a large number of intermediate states accurately in such ultrathin films due to the limited active programming volume. We also note that GeTe/Sb₂Te₃ and Sb₂Te₃/Ge-Sb-Te superlattices may display a relatively low drift with $v \sim 0.002$ –0.009^{40–42}. Nevertheless, their RESET states may be in a partly crystalline state. As seen in Fig. 2e, our CrTe₃ is the only PCM that is immune to resistance drift at all practical operating temperatures for IMC applications.

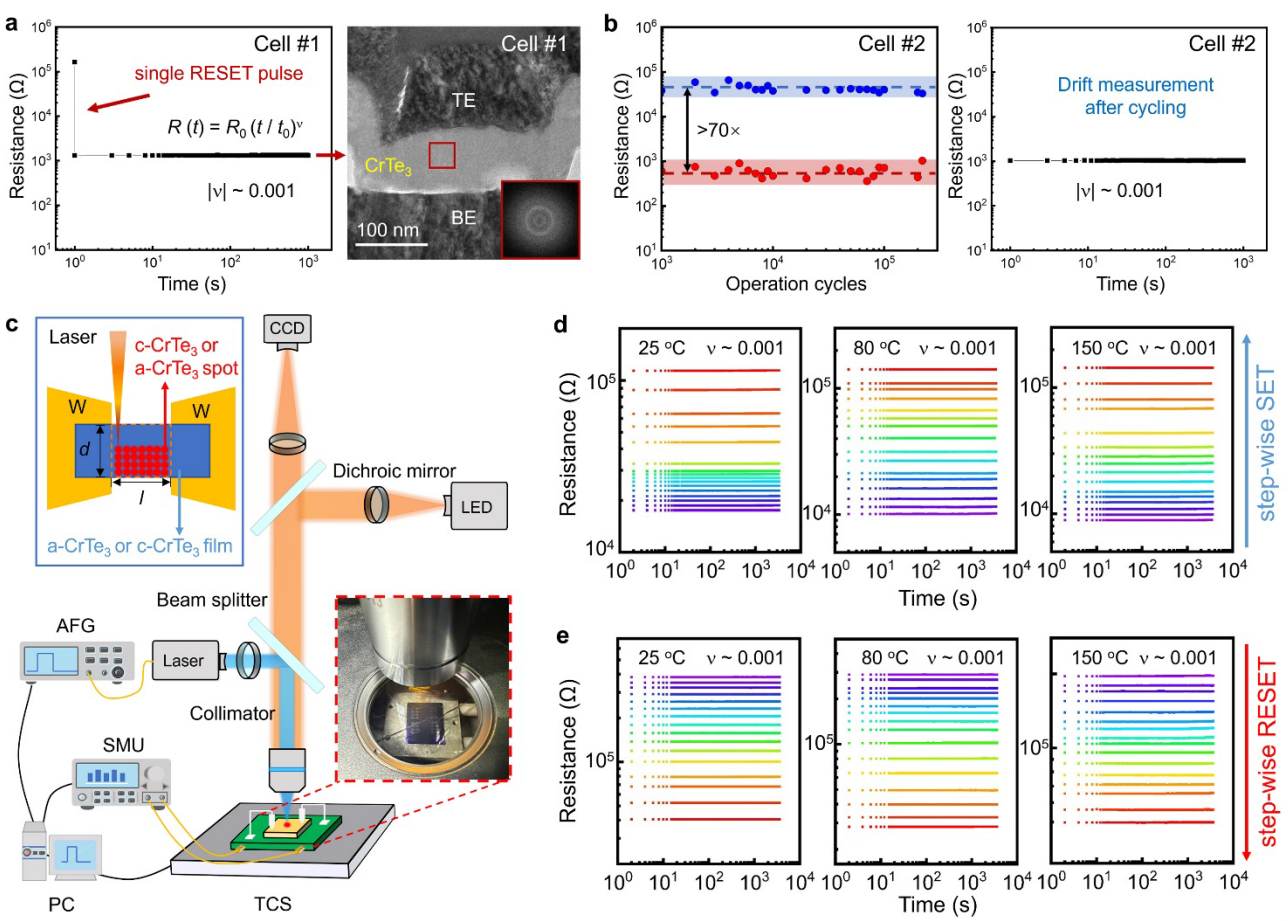


Fig. 3 | Electrical measurements in devices. **(a)** Left panel: A single electrical pulse was applied to fully RESET a confined memory cell and its resistance was monitored immediately at RT. Right panel: the subsequent cross-sectional TEM characterizations of the RESET state, proving that the cell turned fully amorphous (see halos in the FFT pattern). **(b)** The electrically switched cycling test of a second confined cell, and the drift measurement at RT of the full RESET state after cycling for more than 10^5 times. **(c)** The hybrid opto-electro-thermal setup consisted of a nanosecond laser beam with 1 μm spot size (controlled using an arbitrary functional generator, AFG), a source measure unit (SMU) for electrical measurements, and a temperature controller stage (TCS). The top-left inset shows the scheme of optical programming on a bridge-like device. The bottom-right inset shows the photo of the home-made CrTe₃ device. **(d-e)** Using a bridge-like device of $10 \times 20 \mu\text{m}^2$, 16 robust resistance states were obtained at 25, 80 and 150 °C via step-wise SET and step-wise RESET, respectively. Each resistance level was measured after sending two laser pulses.

Deterministic multilevel programming

The essence of multilevel programming in PCM devices is to generate a series of intermediate resistance states, each corresponding to a different ratio of amorphous to crystalline volume. However, fine-tuning the volume fraction of crystalline versus amorphous regions using electrical pulses requires sophisticated device fabrication and control, and is subject to much uncertainty. Here, we developed a

hybrid opto-electro-thermal scheme, which serves the purpose of assessing the multilevel capacity of CrTe₃ in a deterministic way. The precise volume control is achieved via step-wise SET and step-wise RESET laser operations, i.e., generating crystalline or amorphous domains of the same size, one by one in a regular pattern, via laser irradiation on an amorphous or a crystalline thin film (Fig. 3). The actual image of the measurement setups is displayed in Supplementary Fig. S6. Using a bridge-like device covered with as-deposited a-CrTe₃ thin film, we applied laser pulses in the middle part of devices with $l = 20 \mu\text{m}$ and $d = 10 \mu\text{m}$ for a sequential crystallization (step-wise SET) along the vertical direction. After sending every two laser pulses, the electrical resistance was measured and monitored for over 1 hour. During the whole process (> 16 hours), the three devices were continuously held at 25 °C, 80 °C or 150 °C, respectively. As shown in Fig. 3b, each device displayed 16 resistance levels, all with little drift, $v \sim 0.001$. When the holding temperature was increased to 165 °C, the resistance levels can still be well distinguished, despite of a slightly higher v (maximum ~0.004, Supplementary Fig. S7).

Although crystallization rate is not a top-priority parameter to optimize owing to the parallel programming ability of PCM array⁴³, it is still desirable to have relatively fast crystallization to shorten the training time of the neural network. For the above operation, we used laser pulse of 100 ns (90 mW) to generate crystallized a-CrTe₃ domains, as confirmed by Raman spectroscopy measurements in Extended Data Fig. 4a. This crystallization speed may seem surprisingly fast, considering the a-CrTe₃ is rather stable against crystallization with a high activation energy for crystallization, $E_a \sim 3.28$ eV (Extended Data Fig. 4b, higher than the 2.2 eV known for GST). This is because fast crystal growth in CrTe₃ could proceed via relatively quick rearrangement of [CrTe₆] octahedra, given sufficient thermal energy, as the Cr and Te atoms still move collectively, i.e., the robust octahedra do not fall apart into individual atoms that diffuse independently (see AIMD calculations at 300 and 400 °C in Extended Data Fig. 4c).

To RESET the device, stronger laser pulses are needed to heat the PCM above its melting temperature, which, however, could also cause evaporation, as the PCM thin film in the bridge-like device is not fully encapsulated as that in electronic devices. To avoid potential damage induced by strong lasers, we increased the thickness of the capping layer to ~50 nm. We heated the whole bridge-like devices to 350 °C for a complete crystallization of CrTe₃. We then applied shorter and stronger

laser pulses of 70 ns and 130 mW to program the device. We carried out step-wise RESET operation on a c-CrTe₃ device to generate 16 resistance states, and measured their resistance at 25, 80 and 150 °C, respectively (Fig. 3c). Their consistently low drift coefficient $v \sim 0.001$ indicates that the CrTe₃ glass obtained via laser melt-quench behaves the same way as the sputter-deposited and electrical-pulse melt-quenched a-CrTe₃. Many more resistance states can be obtained by either increasing the size of the programming area or reducing the laser wavelength to tailor the amorphous-to-crystalline ratio at a higher resolution. As an attempt, we enlarged the device size to 80×80 μm² and applied the same laser pulses to induce melt-quench amorphization in the crystalline CrTe₃ device. As shown in Extended Data Fig. 5, the multilevel programming of this single device reached 12-bit precision with 4096 distinguishable resistance states (with a resistance separation of ~44 Ω per state) at RT with $v \sim 0.001$. We mapped these resistance values to the weights of a fully connected neural network for image classification simulation (Supplementary Fig. S8), which offered a high accuracy of 97.29% to classify the MNIST datasets, comparable to the software results, 97.31%.

Path-tracking function enabled by stable resistance levels

To highlight the importance of robust resistance levels without resistance drift, we fabricated a 2×2 array of CrTe₃-based bridge-like devices, and integrated the array into a self-made vehicle (Fig. 4a) to realize stable path-tracking function. As shown in Fig. 4b, the control system of this vehicle mainly composed of two grayscale sensors, the device array, the amplifiers and the servomotor. The sensors are symmetrically installed in the front of the vehicle to detect grayscale changes, which provide distinct input voltage signals when detecting black and white. We programmed the 4 well-separated resistance values into the 4 devices via step-wise SET laser operations on as-deposited a-CrTe₃ thin films. The weight (conductance) values of the 4 devices were then mapped into a single-layer neural network (the 2×2 array) as the basic neuromorphic computing unit, performing matrix vector multiplication through Ohm's law and Kirchhoff's law to enable automatic path-tracking⁴⁴. The output current signals from the array were then processed through the transimpedance amplifier and differential amplifier, and were converted into voltage signals again for the final steering and turning actions of the servomotor. The threshold for failure is set as tight as “any weight value changing by more than ±1%”. As shown in Fig. 4c and the Supplementary Video 2, the vehicle tracked the black

path nicely, consistently turning the wheels back to the black path when detecting the white background. This CrTe₃-based path-tracking vehicle still functioned very well after being placed in air for over 1 month, and after heating the control board at 150 °C for over 1 hour. In contrast, if a-GST is used, the resistance drifts by nearly 100% in one hour at room temperature (Supplementary Fig. S5). If heated at 150 °C for 1 hour, a-GST is fully crystallized, causing a complete failure.

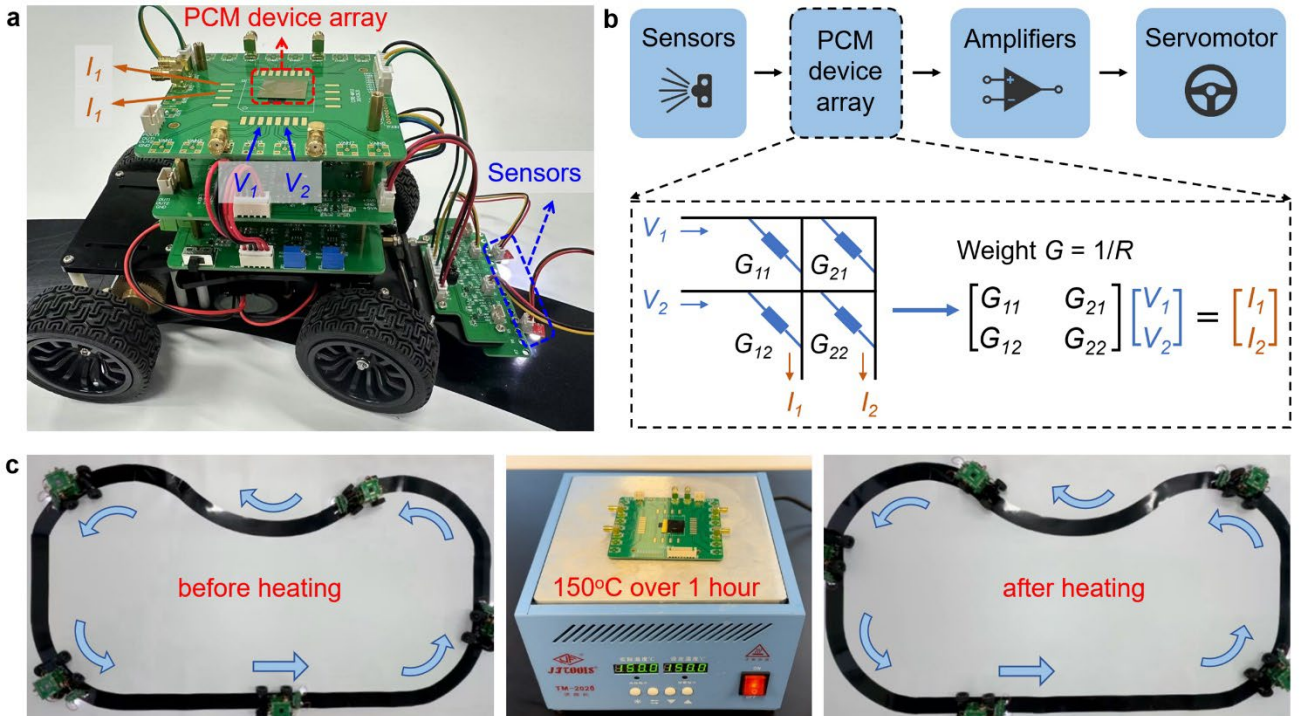


Fig. 4 | The CrTe₃-based path-tracking vehicle. (a) The image of CrTe₃-based path-tracking vehicle. (b) The schematic of the control system with a 2×2 CrTe₃ device array. (c) The path-tracking function was preserved after heating.

Conclusions and outlook

We have designed an unconventional PCM without resistance drift at almost all practical IMC operating temperatures ($T=-200$ °C to 165°C) from the get-go (immediately after the amorphous state was generated) to many hours of aging at each T . The materials science origin of this unprecedented behavior can be summarized as follows. The new a-PCM is characterized by “molecule-like” motifs that are unique in configuration, overwhelmingly predominant throughout the structure, and robust over time. To explore the general validity of such a structural feature, we carried out AIMD simulations and electrical measurement of amorphous TiTe₂ and VTe₂. As shown in Supplementary Fig. S9, the

molecule-like motifs of $[TiTe_6]$ and $[VTe_6]$ octahedra also prevailed, and the measured drift coefficient of a-TiTe₂ and a-VTe₂ thin films was as small as that of a-CrTe₃. Nevertheless, the limited contrast window and the low crystallization temperature of the two alloys render them unfit for practical applications. We also note that not all Te-rich transition metal tellurides should be regarded as molecule-like PCMs. In a very recent work ⁴⁵, a low-drift behavior was found for a-NbTe₄ thin film at room temperature. But no clear molecule-like pattern was observed in the a-NbTe₄ amorphous model obtained via AIMD simulations. Indeed, this low-drift behavior cannot be sustained at slightly elevated temperatures: the drift coefficient quickly increased to ~ 0.082 at 80 °C (see Supplementary Fig. S10).

Overall, our work represents a different avenue towards ultralow resistance drift, by resorting to a glass with truly molecule-like motifs. In contrast with conventional a-PCMs (or some other glass categories) that tend to readily relax towards other adjacent sub-basins (variable motif configurations) across a fairly shallow megabasin in the potential energy landscape, the “molecular-glass-like” a-PCM we designed would stay put in a rather steep basin (see schematic in Extended Data Fig. 6), with little motivation for relaxation and no other desirable motifs to go. The transformation between amorphous and crystalline CrTe₃ via the cooperation of compact and robust octahedra also resulted in a desirable combination of excellent amorphous stability and satisfactorily fast crystallization speed. Future work is anticipated to gain a deeper understanding of this unconventional crystallization scheme via in situ measurements ^{46,47} and machine-learning-facilitated molecular dynamics ⁴⁸. Also, it is necessary to test the multilevel capacity in nanoscale PCM devices ⁴⁹, the endurance beyond million cycles, as well as the device variability of CrTe₃ in a large crossbar array, before it can be put into practical use. Nevertheless, we have demonstrated that CrTe₃ thin films can be produced with wafer-scale homogeneity via a standard sputtering approach, adding no complexity to mass production nor to programming algorithm. Overall, our no-drift discovery achieves the first intrinsically robust a-PCM, offering a front-end materials solution that has the potential to meet the demanding requirements of high-precision multilevel programming at the operation temperatures for both data-centric and edge-computing platforms.

ACKNOWLEDGMENTS

The work is supported by the National Key Research and Development Program of China (2023YFB4404500). W.Z. thanks the support of National Natural Science Foundation of China (62374131). J.-J.W. thanks the support of National Natural Science Foundation of China (62204201).

We acknowledge Dr. Xi Li for useful discussions. We thank Chao Li and Chuansheng Ma for their helps on TEM characterizations, Songquan Yang for his technical support on bridge-like device fabrication, and Weiye Liu for his assistance with the integration of the path-tracking vehicle. We acknowledge the HPC platform of XJTU and the Computing Center in Xi'an for providing computational resources. The authors acknowledge XJTU for hosting their work at CAID. The International Joint Laboratory for Micro/Nano Manufacturing and Measurement Technologies of XJTU is acknowledged.

Author contributions:

W.Z., X.W., and E.M. conceived the idea and designed the experiments and simulations. X.W., J.-J.W. and R.W. carried out most of the experiments with the help of D.X., C.N., Z.Z., C.W., J.Z., W. Zhou., and Z.S. S.S. performed DFT calculations with the help of R.C. and X.S. D.X. and J.-J.W. did the image recognition simulations and the vehicle testing. W.Z., X.W. and E.M. wrote the manuscript with input from J.-J.W. and S.S. All authors discussed the results and approved the submission of the manuscript.

Competing interests:

The authors declare no competing interests.

Data and materials availability:

All data needed to evaluate the conclusions in this paper are included in the paper or the supplementary materials. Several patents (PCT/CN2024/123713, CN 202411271055.6, CN 202411271061.1) on no-drift PCM are under examination.

References:

- 1 Lanza, M. *et al.* Memristive technologies for data storage, computation, encryption, and radio-frequency communication. *Science* **376**, eabj9979 (2022).
- 2 Ielmini, D. & Wong, H.-S. P. In-memory computing with resistive switching devices. *Nat. Electron.* **1**, 333-343 (2018).
- 3 Zhang, W. *et al.* Edge learning using a fully integrated neuro-inspired memristor chip. *Science* **381**, 1205-1211 (2023).
- 4 Ambrogio, S. *et al.* An analog-AI chip for energy-efficient speech recognition and transcription. *Nature* **620**, 768-775 (2023).
- 5 Rao, M. *et al.* Thousands of conductance levels in memristors integrated on CMOS. *Nature* **615**, 823-829 (2023).
- 6 Wang, Z. *et al.* Resistive switching materials for information processing. *Nat. Rev. Mater.* **5**, 173-195 (2020).
- 7 Wang, M. *et al.* Robust memristors based on layered two-dimensional materials. *Nat. Electron.* **1**, 130-136 (2018).
- 8 Boybat, I. *et al.* Temperature sensitivity of analog in-memory computing using phase-change memory. *IEDM Tech. Dig.*, pp. 28.3.1-28.3.4 (2021).
- 9 Jiang, H. *et al.* Sub-10 nm Ta Channel Responsible for Superior Performance of a HfO₂ Memristor. *Sci. Rep.* **6**, 28525 (2016).
- 10 Wuttig, M. & Yamada, N. Phase-change materials for rewriteable data storage. *Nat. Mater.* **6**, 824-832 (2007).
- 11 Zhang, W., Mazzarello, R., Wuttig, M. & Ma, E. Designing crystallization in phase-change materials for universal memory and neuro-inspired computing. *Nat. Rev. Mater.* **4**, 150-168 (2019).
- 12 Cheng, H. Y., Carta, F., Chien, W. C., Lung, H. L. & BrightSky, M. 3D cross-point phase-change memory for

- storage-class memory. *J. Phys. D: Appl. Phys.* **52**, 473002 (2019).
- 13 Song, Z. T. *et al.* High Endurance Phase Change Memory Chip Implemented based on Carbon-doped Ge₂Sb₂Te₅ in 40 nm Node for Embedded Application. *IEDM Tech. Dig.*, pp.27.5.1-27.5.4 (2018).
- 14 Grossier, N. *et al.* ASIL-D automotive-grade microcontroller in 28nm FD-SOI with full-OTA capable 21MB embedded PCM memory and highly scalable power management. *VLSI Tech. Dig.*, pp. 1-2 (2023).
- 15 Kim, H. J. *et al.* Versatile spaceborne photonics with chalcogenide phase-change materials. *npj Microgravity* **10**, 20 (2024).
- 16 Pirovano, A. *et al.* Low-field amorphous state resistance and threshold voltage drift in chalcogenide materials. *IEEE Trans. Electron Dev.* **51**, 714-719 (2004).
- 17 Boniardi, M. *et al.* A physics-based model of electrical conduction decrease with time in amorphous Ge₂Sb₂Te₅. *J. Appl. Phys.* **105**, 084506 (2009).
- 18 Zhang, W. & Ma, E. Unveiling the structural origin to control resistance drift in phase-change memory materials. *Mater. Today* **41**, 156-176 (2020).
- 19 Le Gallo, M. *et al.* Mixed-precision in-memory computing. *Nat. Electron.* **1**, 246-253 (2018).
- 20 Le Gallo, M. *et al.* Precision of bit slicing with in-memory computing based on analog phase-change memory crossbars. *Neuromorph. Comput. Eng.* **2**, 014009 (2022).
- 21 Ghazi Sarwat, S. *et al.* Projected Mushroom Type Phase-Change Memory. *Adv. Funct. Mater.* **31**, 2106547 (2021).
- 22 Ambrogio, S. *et al.* Equivalent-accuracy accelerated neural network training using analogue memory. *Nature* **558**, 60-67 (2018).
- 23 Li, C. *et al.* Understanding phase-change materials with unexpectedly low resistance drift for phase-change memories. *J. Mater. Chem. C* **6**, 3387-3394 (2018).
- 24 Khan, R. S., Dirisagli, F., Gokirmak, A. & Silva, H. Resistance drift in Ge₂Sb₂Te₅ phase change memory line cells at low temperatures and its response to photoexcitation. *Appl. Phys. Lett.* **116**, 253501 (2020).
- 25 Wang, Q. *et al.* Reliable Ge₂Sb₂Te₅ based phase-change electronic synapses using carbon doping and programmed pulses. *J. Materomics* **8**, 382-391 (2022).
- 26 Ding, K. *et al.* Phase-change heterostructure enables ultralow noise and drift for memory operation. *Science* **366**, 210-215 (2019).
- 27 Liu, B. *et al.* Multi-level phase-change memory with ultralow power consumption and resistance drift. *Sci. Bull.* **66**, 2217-2224 (2021).
- 28 Hatayama, S., Song, Y.-H. & Sutou, Y. Low resistance-drift characteristics in Cr₂Ge₂Te₆-based phase change memory devices with a high-resistance crystalline phase. *Mater. Sci. Semicond. Process.* **133**, 105961 (2021).
- 29 Chen, B. *et al.* Suppressing Structural Relaxation in Nanoscale Antimony to Enable Ultralow-Drift Phase-Change Memory Applications. *Adv. Sci.* **10**, 2301043 (2023).
- 30 Raty, J.-Y. *et al.* Aging mechanisms of amorphous phase-change materials. *Nat. Commun.* **6**, 7467 (2015).
- 31 Gabardi, S., Caravati, S., Sosso, G. C., Behler, J. & Bernasconi, M. Microscopic origin of resistance drift in the amorphous state of the phase-change compound GeTe. *Phys. Rev. B* **92**, 054201 (2015).
- 32 Konstantinou, K., Mocanu, F. C., Lee, T. H. & Elliott, S. R. Revealing the intrinsic nature of the mid-gap defects in amorphous Ge₂Sb₂Te₅. *Nat. Commun.* **10**, 3065 (2019).
- 33 McGuire, M. A. *et al.* Antiferromagnetism in the van der Waals layered spin-lozenge semiconductor CrTe₃. *Phys. Rev. B* **95**, 144421 (2017).
- 34 Hatayama, S. *et al.* Inverse Resistance Change Cr₂Ge₂Te₆-Based PCRAM Enabling Ultralow-Energy Amorphization. *ACS Appl. Mater. Interfaces* **10**, 2725-2734 (2018).
- 35 Wang, X. *et al.* Spin glass behavior in amorphous Cr₂Ge₂Te₆ phase-change alloy. *Adv. Sci.* **10**, 2302444 (2023).
- 36 Njoroge, W. K., Woelgens, H.-W. & Wuttig, M. Density changes upon crystallization of Ge₂Sb₂Te₄.74 films.

- J. Vac. Sci. Technol. A* **20**, 230-233 (2002).
- 37 Salinga, M. *et al.* Monatomic phase change memory. *Nat. Mater.* **17**, 681-685 (2018).
- 38 Wimmer, M., Kaes, M., Dellen, C. & Salinga, M. Role of activation energy in resistance drift of amorphous phase change materials. *Front. Phys.* **2**, 75 (2014).
- 39 Navarro, G. *et al.* Trade-off Between SET and Data Retention Performance Thanks to Innovative Materials for Phase-Change Memory. *IEDM Tech. Dig.*, pp.21.5.1-21.5.4 (2013).
- 40 Zhou, L. *et al.* Resistance Drift Suppression Utilizing GeTe/Sb₂Te₃ Superlattice-Like Phase-Change Materials. *Adv. Electron. Mater.* **5**, 1900781 (2019).
- 41 Khan, A. I. *et al.* Ultralow-switching current density multilevel phase-change memory on a flexible substrate. *Science* **373**, 1243-1247 (2021).
- 42 Wu, X. *et al.* Novel nanocomposite-superlattices for low energy and high stability nanoscale phase-change memory. *Nat. Commun.* **15**, 13 (2024).
- 43 Burr, G. W. *et al.* Large-scale neural networks implemented with non-volatile memory as the synaptic weight element: Comparative performance analysis (accuracy, speed, and power). *IEDM Tech. Dig.*, pp.4.4.1-4.4.4 (2015).
- 44 Wang, C. *et al.* A Braitenberg Vehicle Based on Memristive Neuromorphic Circuits. *Adv. Intell. Syst.* **2**, 1900103 (2019).
- 45 Shuang, Y. *et al.* NbTe₄ Phase-Change Material: Breaking the Phase-Change Temperature Balance in 2D Van der Waals Transition-Metal Binary Chalcogenide. *Adv. Mater.* **35**, 2303646 (2023).
- 46 Zalden, P. *et al.* Femtosecond X-ray diffraction reveals a liquid-liquid phase transition in phase-change materials. *Science* **364**, 1062-1067 (2019).
- 47 Jiang, T.-T. *et al.* In situ characterization of vacancy ordering in Ge-Sb-Te phase-change memory alloys. *Fundam. Res.* **4**, 1235-1242 (2024).
- 48 Zhou, Y., Zhang, W., Ma, E. & Deringer, V. L. Device-scale atomistic modelling of phase-change memory materials. *Nat. Electron.* **6**, 746-754 (2023).
- 49 Kim, W. *et al.* Confined PCM-based Analog Synaptic Devices offering Low Resistance-drift and 1000 Programmable States for Deep Learning. *VLSI Tech. Dig.*, T66-T67 (2019).

Methods

Synthesis and structural characterizations

The CrTe₃ thin films of ~50–150 nm were deposited on 4-inch SiO₂/Si substrates at room temperature with a pure Cr target and a pure Te target in high vacuum via AJA ORION 8 (base pressure of less than $\sim 1 \times 10^{-5}$ Pa). The deposition rate was set to 9.5 nm min⁻¹. The chemical composition of the sputtered films was determined to be approximately Cr_{25.4}Te_{74.6} by the energy-dispersive X-ray (EDX) experiments. The structures of the as-deposited and post-annealed thin films were investigated by XRD with Cu K α radiation (Bruker D8 ADVANCE). The TEM specimens were prepared by a dual beam FIB system (Helios NanoLab 600i, FEI) with a Ga ion beam operated at 30 kV. A Pt protective layer was deposited above the CrTe₃ thin film to mitigate potential damages from Ga ions during the FIB lift-out and thinning processes. The TEM experiments were performed on a Talos-F200X operated at 200 kV. The STEM-HAADF imaging and EDX mapping experiments were performed on a JEOL ARM300F STEM with a probe aberration corrector, operated at 300 kV. Raman spectra were collected using Renishaw inVia Qontor with a solid-state 532 nm laser for the excitation, where the laser power was set as 0.25 mW, and an exposure time of 2 seconds with 50 cycles was used.

Fabrication of devices and the vehicle

Two lithography processes were adopted for the fabrication of the bridge-like devices. The first lithography process was applied to pattern the layer of metal electrode on a SiO₂ wafer using a UV lithography machine (SUSS MJB4). The tungsten electrodes of 30 nm thickness were deposited on the patterned substrate via magnetron sputtering followed by lift-out process. The second lithography process was applied to pattern the PCM layer. The deposited CrTe₃ layer (~50 nm) was slightly thicker than that of the tungsten electrodes in order to ensure the connectivity of the device. A ZnS-SiO₂ protective layer with a thickness of 20 nm was deposited on top of the surface. Both lithography processes were done using a negative photoresist (AZ5214E). The 2×2 CrTe₃ device array was fabricated and integrated on a custom-printed circuit board (PCB) using a wire bonder (TPT HB10). The vehicle consisted of two grayscale sensors, a CrTe₃ array, amplifiers and a motor system (including servomotor and engine), batteries and the vehicle body. The servomotor performed different steering actions directed by the CrTe₃-based control system.

Electrical measurements

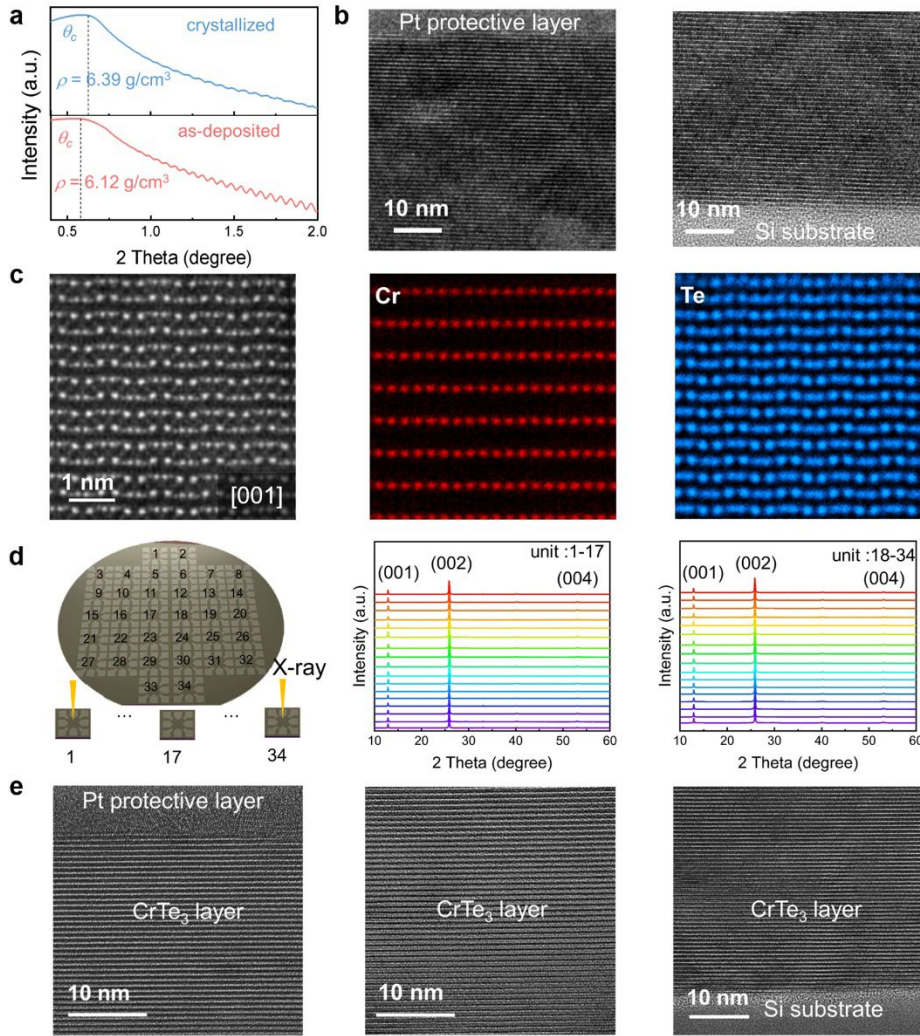
The home-made electrical testing system was constructed by connecting the Keithley 2636B source meter and the Instec mK200 hot stage with a temperature accuracy of 0.001 °C. The sheet resistance of the CrTe₃ films as a function of temperature was measured with a heating rate of 10 °C / min under Ar protection. The probe electrodes were made of tungsten. For the electrical measurements of 34 units on the wafer, we first broke down these units from the wafer, and then repeated the sheet resistance measurement on each of them. The PPMS instrument (Quantum Design DynaCool) was used for the Hall effect measurement at room temperature, and the low-temperature resistance measurements between –50 to –200 °C. The electrical measurements of confined memory devices were performed using the Keithley 2400C source meter (measuring cell resistance) and the Tektronix AWG5002B pulse generator (generating voltage pulse). The self-built opto-electro-thermal platform was equipped with Stradus 488-25 lasers, arbitrary function generator (AFG 31000 SERIES), the optical path system, Keithley 2636B source meter, Instec mK200 hot stage and a computer. The wavelength of the applied laser was fixed at 488 nm. The source meter records the resistance values continuously so that any change in resistance can be monitored in real time upon multilevel programming. Slight numerical difference in the electrical resistance value of the amorphous (or crystalline) state is expected for different device setups, in which the film thickness, length, type of electrodes, amorphous-to-crystal ratio, orientation of the crystal, etc., can lead to some resistance variations.

Ab initio calculations

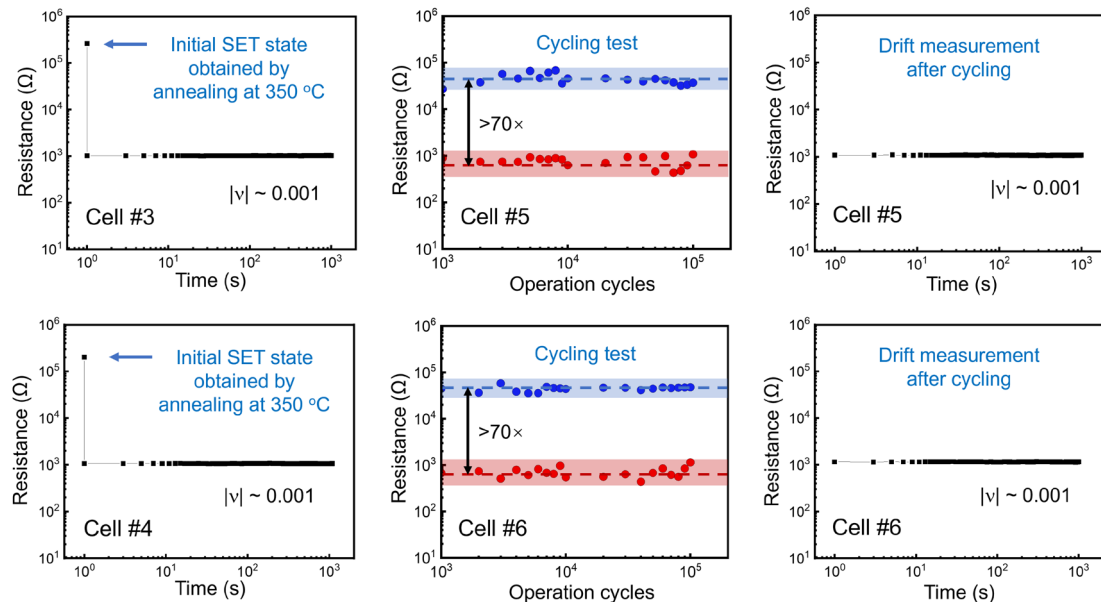
We carried out DFT-based AIMD simulations using the second-generation Car–Parrinello molecular dynamics scheme ⁴⁶ as implemented in the CP2K package ⁴⁷. The Kohn–Sham orbitals were expanded by a double- and triple-zeta plus polarization Gaussian-type basis set for Cr and Te, and the charge density was expanded in plane waves with a cutoff of 300 Ry. The Goedecker–Teter–Hutter (GTH) pseudopotentials ⁴⁸ and Perdew–Burke–Ernzerhof (PBE) functional ⁴⁹ with van der Waals (vdW) correction based on the Grimme’s D3 method ⁵⁰ were applied, and the spin-polarization was considered using α and β orbitals without spin restriction. The AIMD calculations were carried out using the canonical ensemble (NVT) with a time step of 2 fs. To generate a-CrTe₃, 50 Cr atoms and 150 Te atoms were randomly arranged in a cubic cell. The model was heated above 3000 K to remove all possible crystalline order, and were then quenched down to ~1200 K in 10 ps. After an AIMD run at ~1200K

for 30 ps, the model was then quenched down to 0 K with a cooling rate of 12.5 K ps⁻¹. To collect structural data at different holding temperatures, the corresponding snapshots within the cooling process were picked out for a separate 50-ps AIMD run at the respective holding temperature. Three amorphous models with independent thermal history were calculated in both crystalline and amorphous densities, respectively. The structural relaxation and further spin-polarized density of states analyses at 0 K were conducted using the VASP code⁵¹ with PBE functional, vdW-D3 correction, and the projector augmented-wave (PAW) pseudopotentials⁵². The energy cutoff was set as 450 eV. Each amorphous model contained 50 Cr atoms and 150 Te atoms, and its Brillouin zone was sampled using Γ point. For c-CrTe₃, the unit cell contained 8 Cr atoms and 24 Te atoms, and its Brillouin zone was sampled using a 2×2×4 k-point mesh.

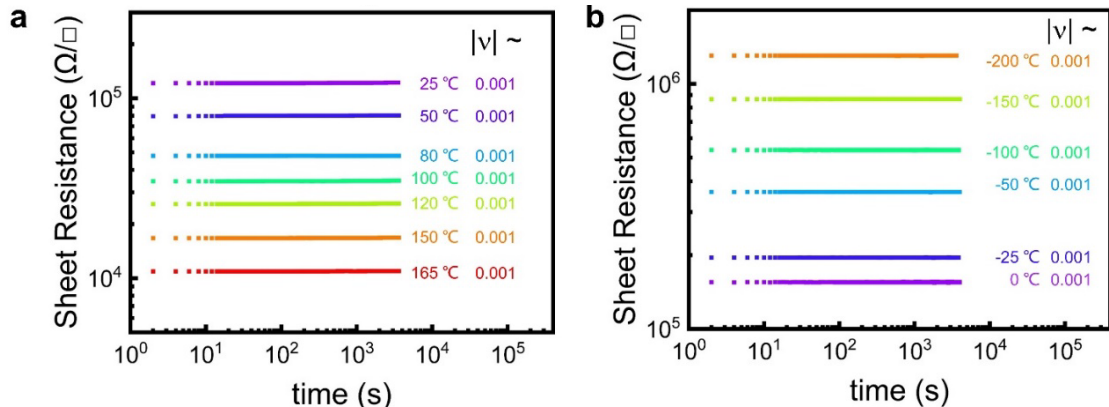
50. T. Kühne, M. Krack, F. Mohamed, M. Parrinello, *Phys. Rev. Lett.* **98**, 066401 (2007).
51. T. D. Kühne, *et al.*, *J. Chem. Phys.* **152**, 194103 (2020).
52. S. Goedecker, M. Teter, J. Hutter, *Phys. Rev. B* **54**, 1703 (1996).
53. J. P. Perdew, K. Burke, M. Ernzerhof, *Phys. Rev. Lett.* **77**, 3865-3868 (1996).
54. S. Grimme, J. Antony, S. Ehrlich, H. Krieg, *J. Chem. Phys.* **132**, 154104 (2010).
55. G. Kresse, J. Furthmüller, *Phys. Rev. B* **54**, 11169 (1996).
56. P. E. Blöchl, *Phys. Rev. B* **50**, 17953-17979 (1994).



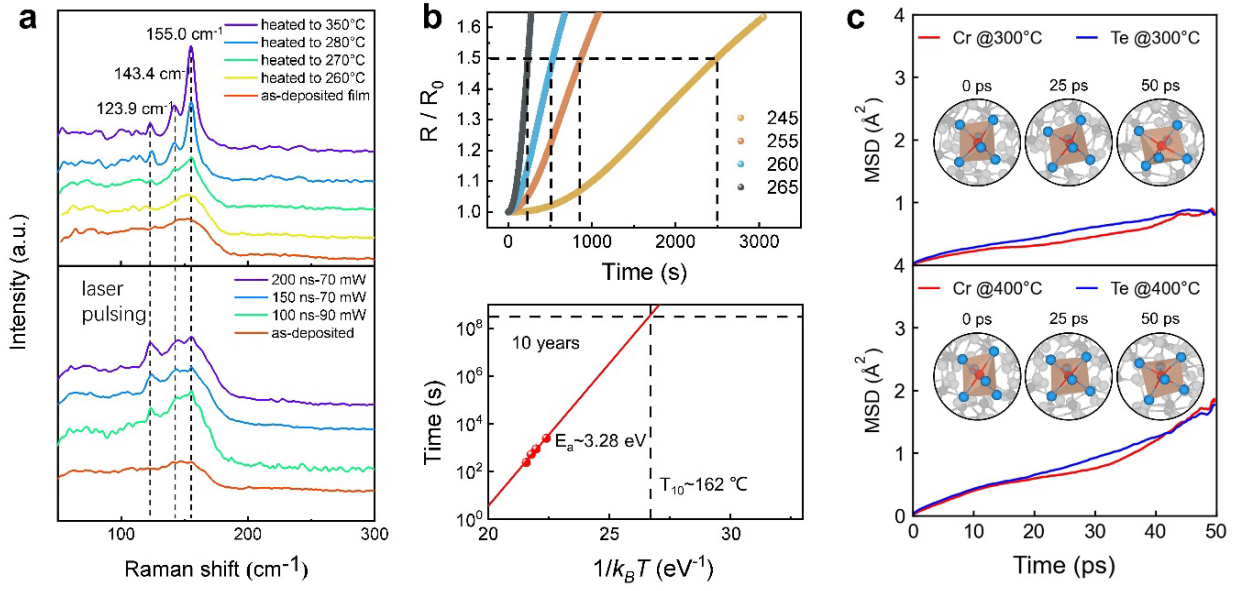
Extended Data Fig. 1 | Structural characterizations of CrTe₃ thin films. (a) The XRR spectrum of as-deposited films and crystallized CrTe₃ films of ~150 nm. (b) The TEM images near top Pt protective layer and the Si substrate of crystallized CrTe₃ film of ~150 nm. (c) The atomic-scale HAADF image of crystalline CrTe₃ viewed in the [001] direction and its corresponding EDS mapping of Cr and Te. The intensity of spots in the HAADF image is approximately proportional to the square of the averaged atomic number Z of each column along the view direction, therefore, the Te (Z = 54) columns look brighter than the Cr (Z = 24) columns. (d) The measured XRD patterns over 34 locations on the 4-inch wafer. (e) The TEM images recorded at different locations of crystallized CrTe₃ film of ~50 nm. No clear grain boundary can be observed over >5 μm lateral direction. The film thickness along the beam incidence direction was ~80 nm for all TEM specimens we prepared.



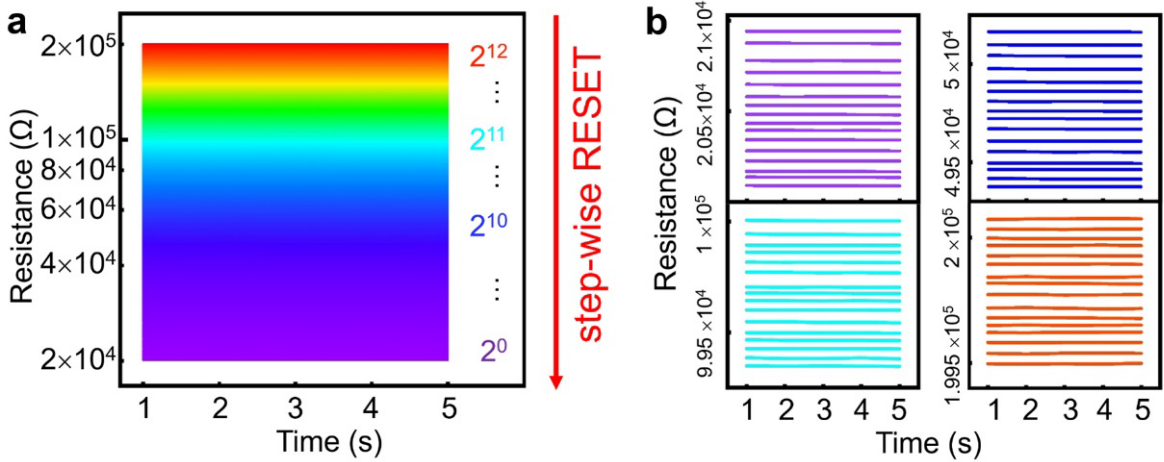
Extended Data Fig. 2 | The drift measurements after the initial RESET operation, the cycling endurance test itself, and the drift measurements of the full RESET state after cycling at RT. Electrical measurements of four additional confined memory cells confirmed the no-drift behavior of the RESET state.



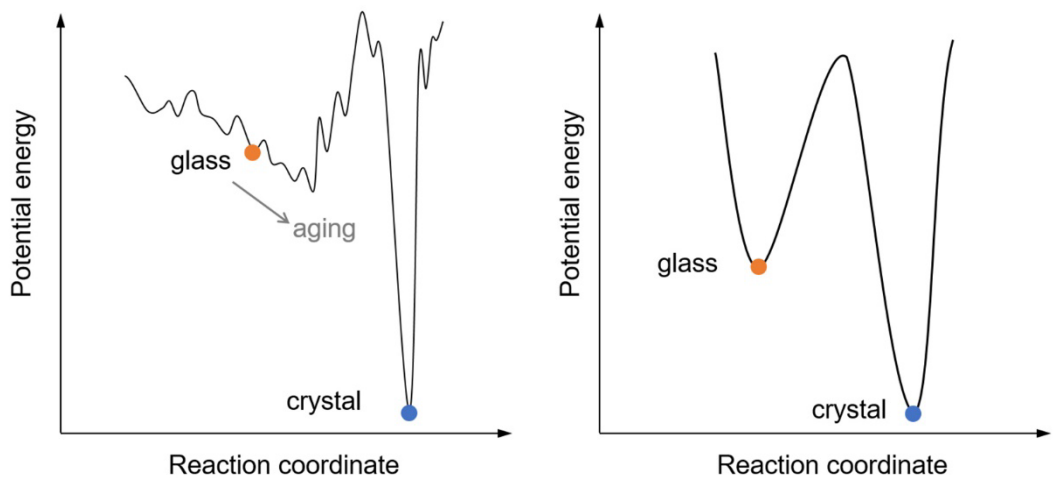
Extended Data Fig. 3 | The resistance drift measurements of the crystallized CrTe₃ thin films, each conducted at a different holding temperature (a) at or above RT, and (b) at 0 °C or below.



Extended Data Fig. 4| Switching and dynamics. (a) The measured Raman spectrum of the as-deposited film, and the films being heated to 260 °C, 270 °C, 280 °C and 350 °C, respectively (upper panel). The Raman spectrum measured at the laser-irradiated spots of the films (lower panel). (b) The electrical resistance of as-deposited CrTe₃ films measured at 245 °C, 255 °C, 260 °C and 265 °C, respectively (upper panel). The extrapolated 10-year data retention temperature $T_{10\text{-year}}$ and the estimated activation energy E_a of crystallization for a-CrTe₃ (lower panel). (c) The mean squared displacement (MSD) curves of a-CrTe₃ at 300°C and 400°C via AIMD calculations. The insets show a series of snapshots of a typical Cr[Te₆] octahedron taken at 0, 25 and 50 ps of the AIMD trajectories at respective temperatures. The Cr[Te₆] octahedron was robust, and the associated 1 Cr atom and 6 Te atoms moved collectively. At both holding temperatures, the fraction of Cr atoms in Cr[Te₆] octahedron is over 90% despite of thermal fluctuations.



Extended Data Fig. 5| Deterministic multilevel programming. (a) Using a larger device of $80 \times 80 \mu\text{m}^2$, 4096 (2^{12}) resistance states were obtained after step-wise RESET at RT. Each resistance level was measured after sending one laser pulse. (b) The zoom-in images of multiple resistance states at different resistance windows. The drift coefficient of all the above resistance states was measured as $v \sim 0.001$.



Extended Data Fig. 6| Schematic of the potential energy landscape. A substantial difference is expected for conventional PCMs and our new molecule-like PCMs (see text for explanation).

Supplementary Information

for

No-drift phase-change memory alloy for neuromorphic computing

Xiaozhe Wang^{1,#}, Ruobing Wang^{2,#}, Suyang Sun^{1,#}, Ding Xu¹, Chao Nie¹, Zhou Zhou¹, Chenyu Wen¹, Junying Zhang¹, Ruixuan Chu¹, Xueyang Shen¹, Wen Zhou¹, Zhitang Song², Jiang-Jing Wang^{1,*}, En Ma^{1,*}, Wei Zhang^{1,*}

¹Center for Alloy Innovation and Design (CAID), State Key Laboratory for Mechanical Behavior of Materials, Xi'an Jiaotong University, Xi'an, 710049, China.

²National Key Laboratory of Materials for Integrated Circuits, Shanghai Institute of Microsystem and Information Technology, Chinese Academy of Sciences, Shanghai 200250, China

#These authors contributed equally to this work.

*Emails: j.wang@xjtu.edu.cn, maen@xjtu.edu.cn, wzhang0@mail.xjtu.edu.cn

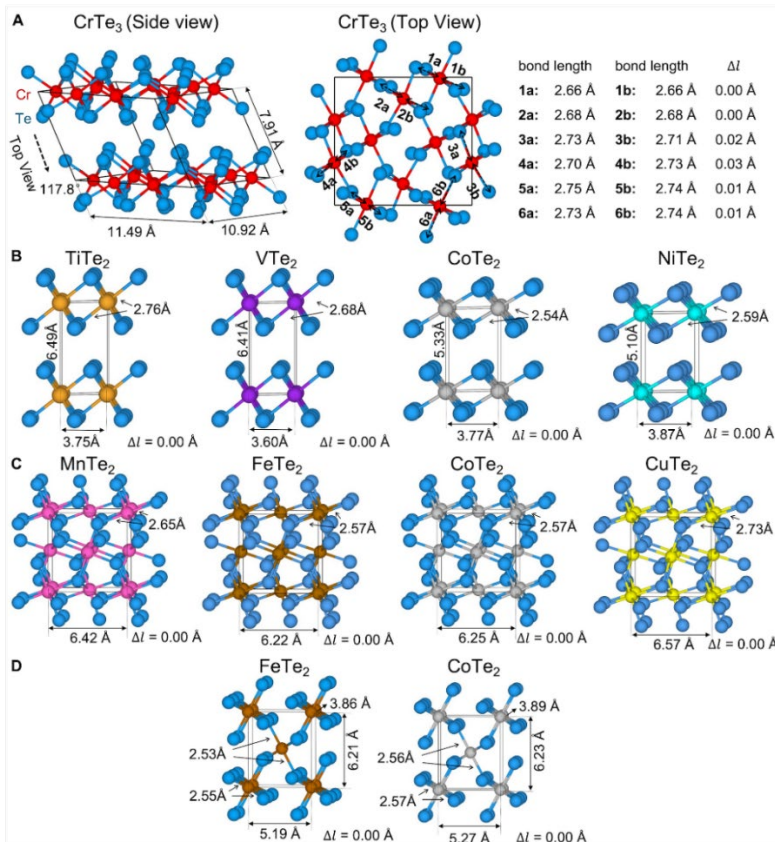


Figure S1. The DFT-optimized crystal structures of the Te-rich 3d-transition-metal tellurides found in the inorganic crystal structure database (ICSD). (a) Monoclinic CrTe₃. The bonds along each direction were marked. (b) Hexagonal TiTe₂, VTe₂, CoTe₂ and NiTe₂. (c) Cubic MnTe₂, FeTe₂, CoTe₂ and CuTe₂. (d) Tetragonal FeTe₂ and CoTe₂.

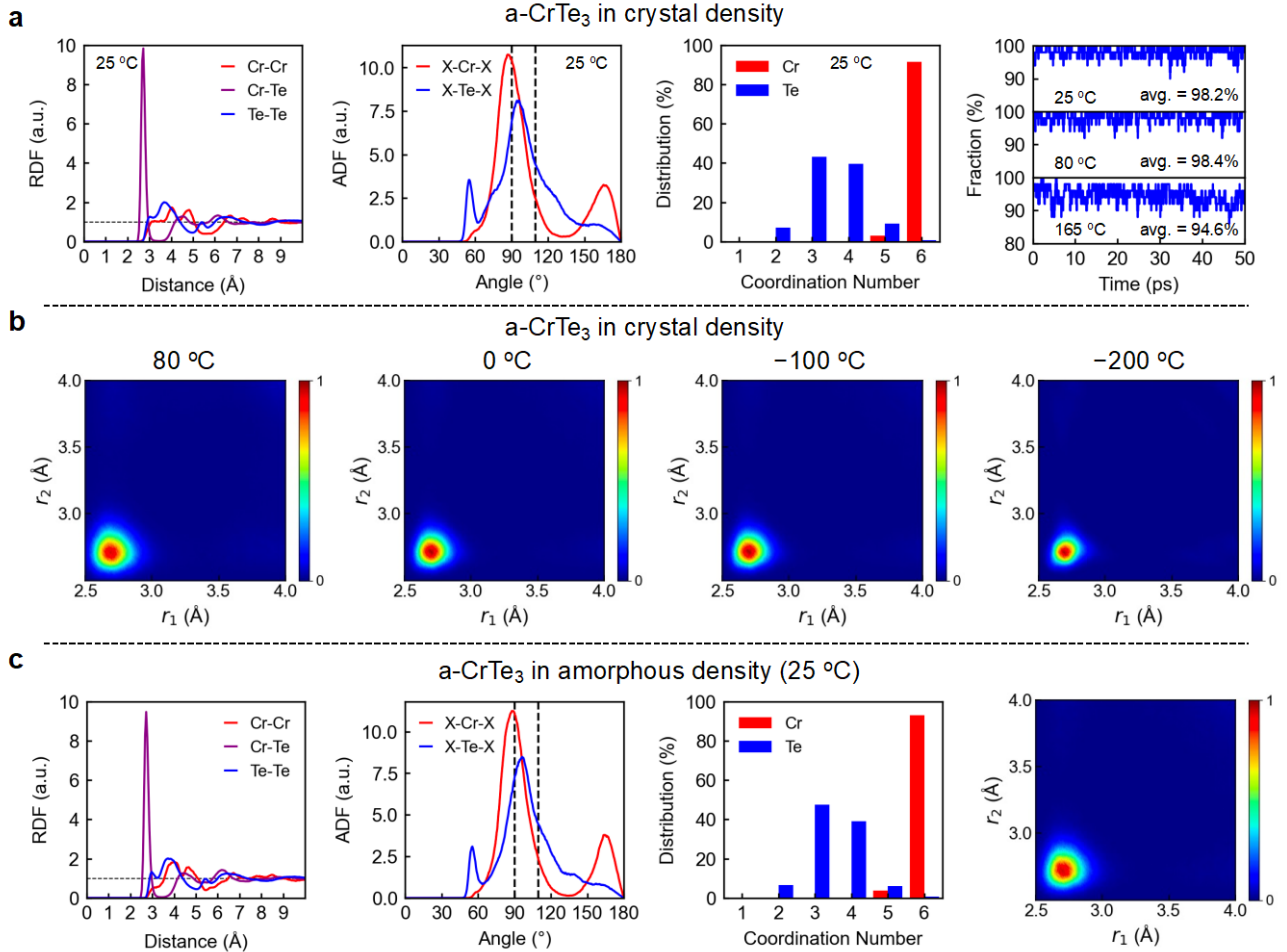


Figure S2. Structural analyses of a-CrTe₃ models at different temperatures. The interatomic cutoffs of 2.9, 3.4 and 3.2 Å were used for Cr-Cr, Cr-Te, and Te-Te, respectively. (a) The radial distribution function (RDF), angular distribution function (ADF), the distribution of coordination number (CN), and changes in number density of [CrTe₆] octahedra over time of the a-CrTe₃ model in crystal density. The number of [CrTe₆] octahedron was determined by calculating the bond order parameter $q = 1 - 3/8 \sum_{x>y} (1/3 + \cos \theta_{xmy})$, where θ_{xmy} represents the bond angle of the center atom m with its two neighboring atoms x and y. The fraction of [CrTe₆] octahedra at 165 °C can be increased, if the Cr-Te cutoff was increased to account for the stronger thermal vibrations at such T. (b) The ALTBC plots of the a-CrTe₃ model in crystal density calculated at 80°C, 0°C, -100°C and -200°C. (c) The RDF, ADF, CN distribution, and ALTBC of CrTe₃ models in amorphous density calculated at 25°C.

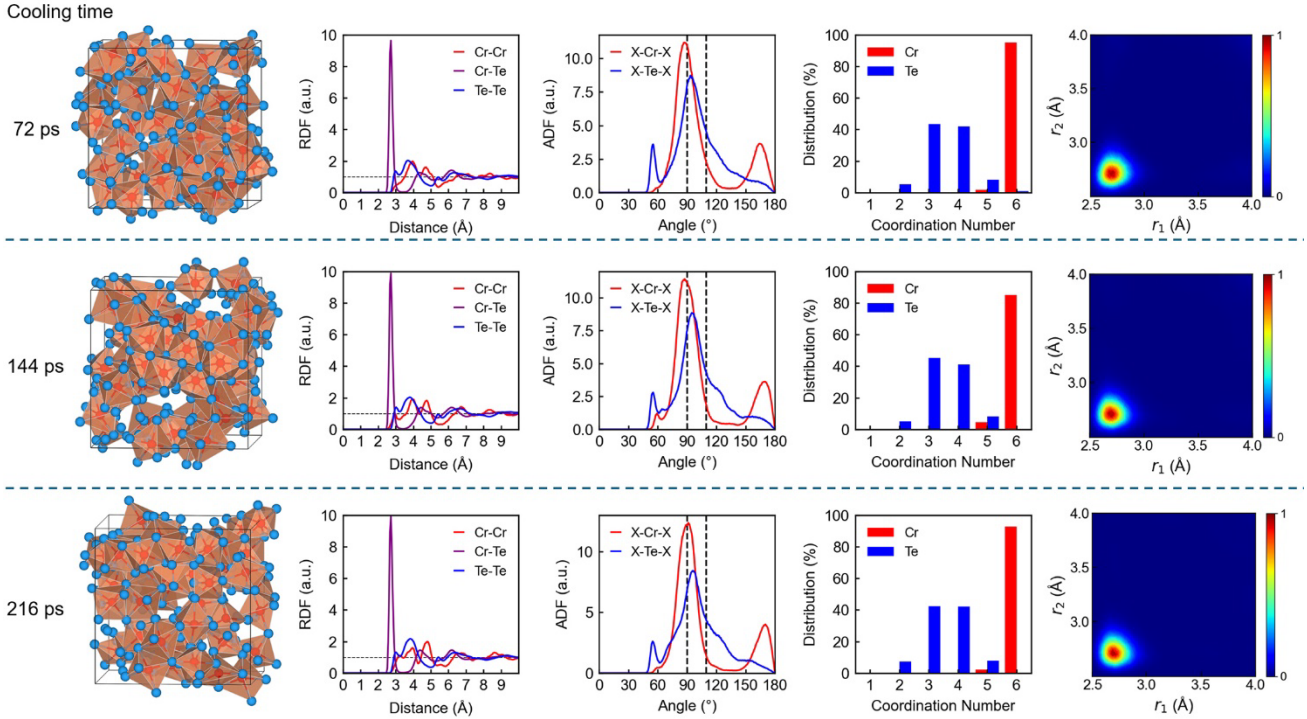


Figure S3. The molecule-like structural features of a-CrTe₃ remained basically the same upon cooling from 1200 K to 300 K with longer cooling time, namely, 144 ps and 216 ps as compared to 72 ps (used in Figure 1).

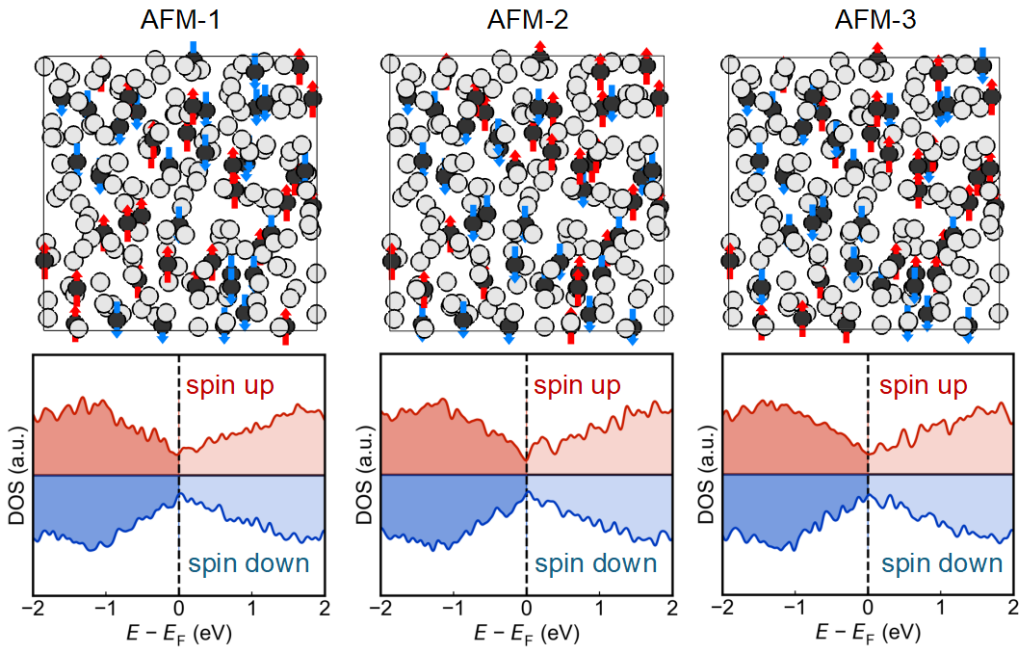


Figure S4. The a-CrTe₃ model calculated in three antiferromagnetic configurations (equal amount of Cr atoms assigned with spin up and spin down moments). The three a-CrTe₃ models were further relaxed. The Cr and Te atoms are rendered in black and gray circles. The red and blue arrows mark the Cr atomic moment directions, respectively. These models were ~5.2 meV/atom higher in energy than the ferromagnetic a-CrTe₃ model, and ~106.2 meV/atom higher than the antiferromagnetic c-CrTe₃ model, shown in Fig. 1.

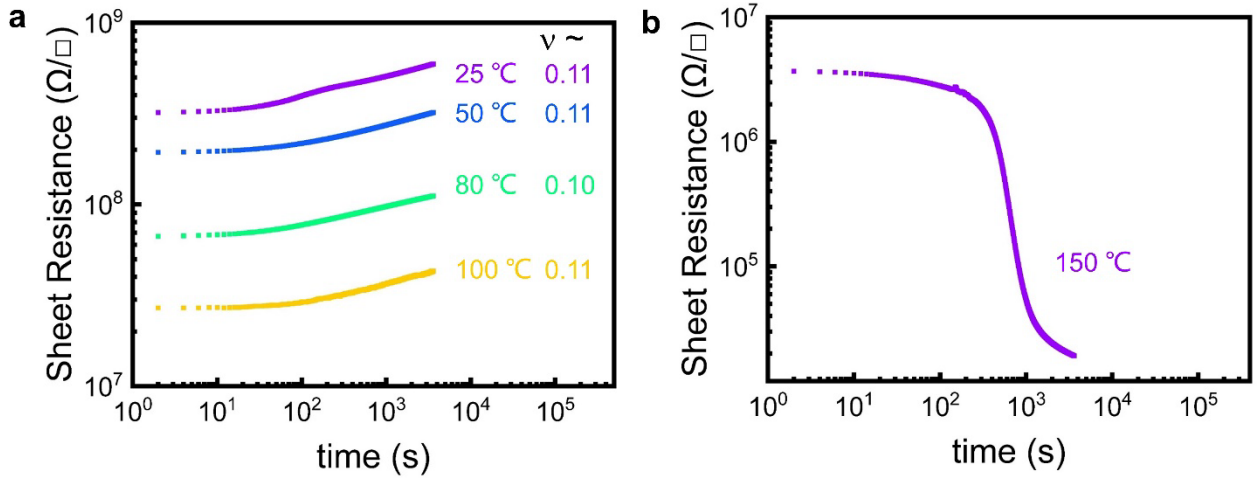


Figure S5. The electrical characterizations of a-GST thin films. (a) Resistance drift tests were performed on at 25, 50, 80 and 100°C, respectively, and the obtained drift coefficients were found between 0.10 and 0.11. (b) The a-GST thin film was crystallized quickly at 150°C.

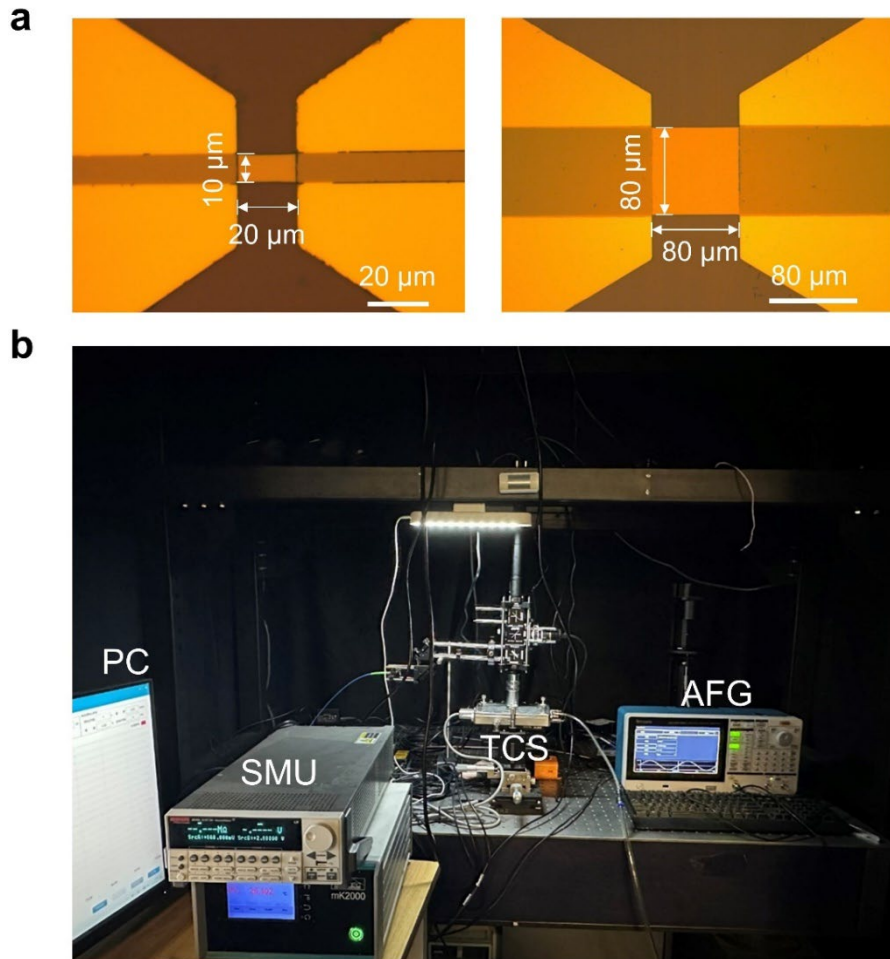


Figure S6. (a) The optical images of the bridge-like devices. Two bridge device structures with different size of $20 \times 10 \mu\text{m}^2$ and $80 \times 80 \mu\text{m}^2$ were shown. (b) A photo of the self-built opto-electro-thermal testing platform.

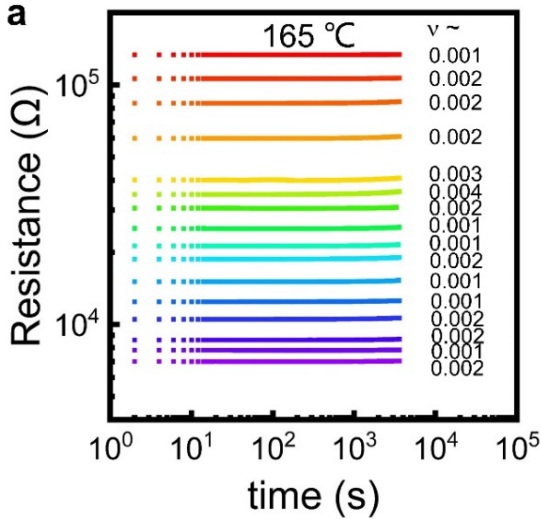


Figure S7. The 16 resistance states obtained using the small bridge-like device, showing a maximum drift coefficient ~ 0.004 at 165 °C.

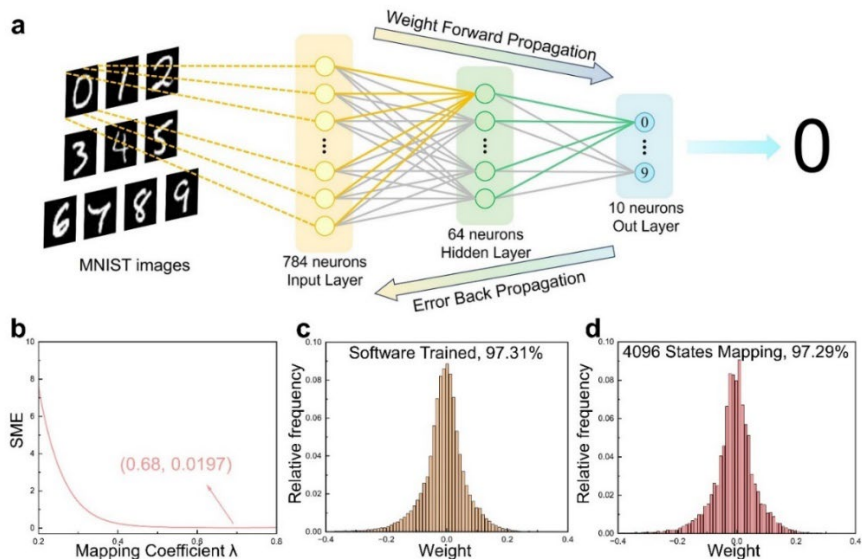


Figure S8. MNIST recognition simulations using the CrTe₃ device data. (a) A fully connected neural network model with 784 input layer neurons, 64 hidden layer neurons, and 10 output layer neurons was built and trained through Python Pytorch to obtain the optimal weight matrix. The experimentally measured 4096 states of the CrTe₃ device data (Fig. 4c) were mapped into this optimal weight matrix by introducing square mapping error (SME) function, and these conductance values were normalized to be between 1 and -1. (b) The calculated SME as a function of mapping coefficient λ , $SME = \min\{\sum[\lambda G - W]^2\}$. A minimum SME, 0.0197, was obtained at $\lambda = 0.68$. The weight distribution and accuracy of recognition and classification (c) after software training, 97.31%, and (d) via mapping the CrTe₃ device data, 97.29%.

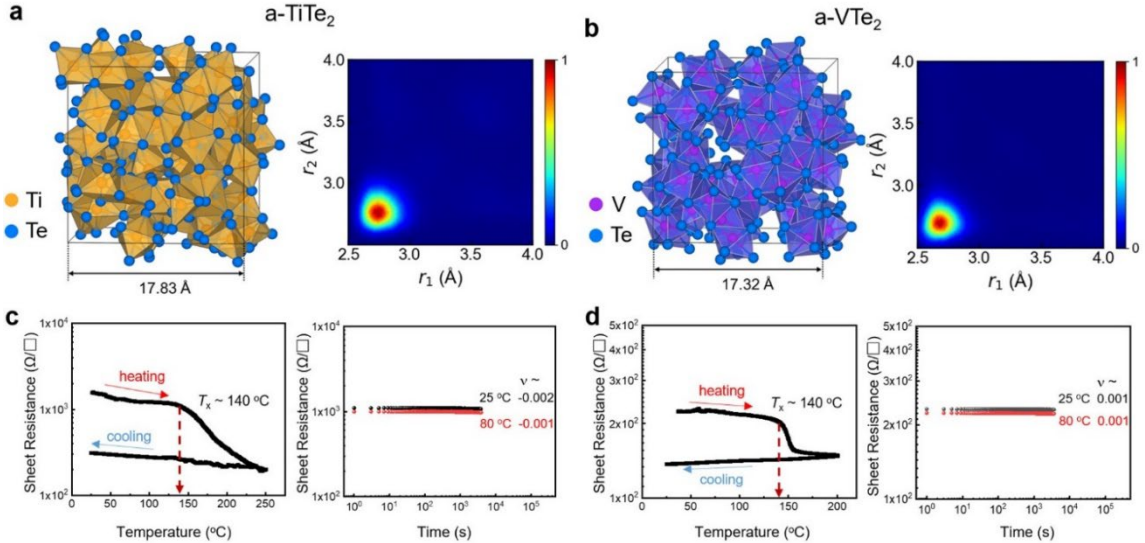


Figure S9. The AIMD modeling and electrical measurements of a-TiTe₂ and a-VTe₂. (a) A snapshot of a-TiTe₂ and the ALTBC plot of a-TiTe₂ annealed at 25 °C. (b) A snapshot of a-VTe₂ and the ALTBC plot of a-VTe₂ annealed at 25 °C. The Ti, V and Te atoms are rendered with orange, purple and blue spheres. The as-deposited (c) TiTe₂ and (d) VTe₂ thin film of ~50 nm both showed a T_x of ~140 °C upon heating. Their drift coefficient values at 25 °C and 80 °C were comparable to those of a-CrTe₃ thin films.

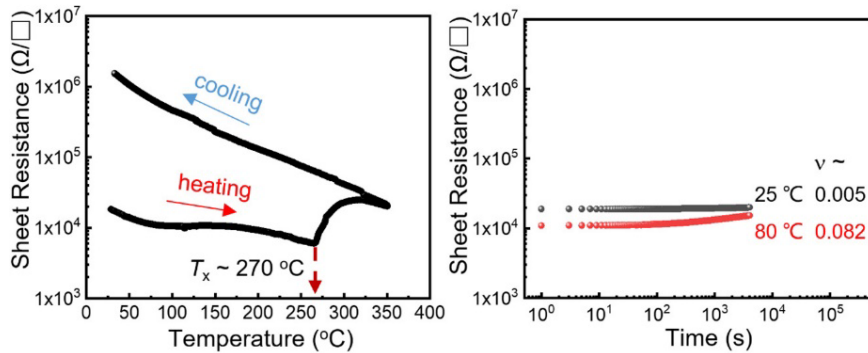


Figure S10. Electrical measurements of as-deposited NbTe₄ thin films of ~50 nm. The R-T curve showed an inverse contrast window upon crystallization. The drift coefficient v of a-NbTe₄ thin film was measured to be ~0.005 at 25 °C, markedly increasing to ~0.082 at 80 °C.